International Forum on Aeroelasticity and Structural Dynamics
IFASD 2024
17-21 June 2024, The Hague, The Netherlands

EFFECT OF GUST MODELS ON THE RESPONSE PREDICTION OF A VERY FLEXIBLE WIND TUNNEL WING MODEL

Stefanie Düssler[1], Christoph Mertens[2] and Rafael Palacios[1]

[1]Imperial College London
SW7 2AZ London, United Kingdom
s.dussler20@imperial.ac.uk
r.palacios@imperial.ac.uk

[2]Royal Netherlands Aerospace Centre
Anthony Fokkerweg 2, 1059CM Amsterdam, The Netherlands
christoph.mertens@nlr.nl

Keywords: very flexible wing, dynamic gust response, gust vane modelling

Abstract: The modelling capabilities of a nonlinear aeroelastic simulation toolbox regarding its gust response prediction of a very flexible wing are exercised against the wind tunnel experiment of the Delft-Pazy wing. Sectional force corrections are employed to capture low Reynolds number effects and the static lift deficiency at high angles of attack due to the onset of separation. With these corrections, both the steady and dynamic wing deformations match the experimental results well. We further simulated the unsteady inflow to the Delft-Pazy wing that is produced by the gust vanes in the wind tunnel simultaneously with the wing itself, instead of using a frozen gust model. The results of this simulation indicate a considerable influence of the wing's presence on the gust velocity that was measured upstream of the wing in the wind tunnel experiment. The structural response differs only slightly utilizing the two different gust models, confirming the frozen gust model being a valid assumption for the moderately large deflections of the Delft-Pazy wing. Possible geometrical nonlinear effects are assessed and are found to become apparent for this wing because of the nonlinear aeroelastic equlibrium but not the gust excitation itself.

1 INTRODUCTION

Future aircraft are expected to have much higher aspect ratio wings, resulting in higher flexibility, and thus larger deformation. A question arises of which methods can sufficiently predict the resulting aeroelastic and possible nonlinear dynamics while being computationally affordable. This has recently been addressed in the Large Deflection Working Group, part of the third Aeroelastic Prediction Workshop, in the frame of flutter prediction studies [1]. The focus has been on the Pazy wing, a very flexible benchmark model, designed and experimentally tested at Technion [2, 3]. The structural dynamic characteristics and aerodynamic features of these flexible structures can also change significantly in the event of strong gust-induced deformation [4].

Ref. [5] presents a slightly altered design of the Pazy wing, with the same dimensions but an even higher flexibility, which was tested in a low-speed wind tunnel facility at TU Delft and is henceforth referred to as *Delft-Pazy wing*. Their focus has been on characterizing periodic gust responses experimentally using non-intrusive measurements of the flow field and the structural deformations, using a volumetric particle tracking velocimetry method. The periodic gust

was generated in the wind tunnel with two oscillating gust vanes upstream of the wing. The accurate experimental characterization of such a gust inflow is sometimes not trivial due to the interaction of the gust with the highly-deformed experimental model that is being tested and other experimental setup components that alter the inflow with respect to an undisturbed flow. To characterize the gust that was realized in the wind tunnel experiment of the Delft-Pazy wing, the inflow velocity variation has been analyzed at 0.75 chord lengths upstream of the wing in Ref. [5]. In Ref. [6], a validation of a 3D free wake panel method has been obtained using these experiments, the results of which gave rise to the suspicion of an erroneous measurement of the gust velocity magnitude and a phase shift due to the influence of the unsteady wing motion on the inflow velocity at the selected gust inflow measurement location.

We aim to investigate this hypothesis by modelling the gust itself, simulating the oscillating gust vanes and their shed wakes representing the gust. This gust vane modelling has already been modelled using the UVLM in Ref. [7], which also compared the resulting induced gust velocities to 2D CFD simulations [8]. We now not only model the gust vanes but simultaneously the Delft-Pazy wing. This novel approach also allows us to explore potential limitations of the frozen gust assumption. Additionally, this serves to validate the nonlinear aeroelastic simulation environment SHARPy regarding its gust response prediction. Lastly, it might be of interest for potential future benchmark problems of the expected nonlinear effects becoming apparent for different gust-induced deformation amplitudes and frequencies.

The paper is structured such that we introduce the numerical methods used for fully nonlinear aeroelastic simulations and for the linearization and order-reduction process in section 2. Next, the Delft-Pazy wing and the experimental setup are briefly introduced, followed by a description of the computational implementation (section 3). In section 4, we evaluate the frozen gust response prediction capabilities of the nonlinear aeroelastic solver by comparing it against the experimental results. Subsequently, we discuss the results obtained modelling both the Delft-Pazy wing and the gust vanes by evaluating the induced velocity field and the dynamic wing deformation response in section 5. Last, we evaluate the effect on structural nonlinearities present in section 6.

2 AEROELASTIC COMPUTATIONAL METHODS

The nonlinear aeroelastic simulations are performed with the open-source simulation environment SHARPy [9]. SHARPy couples a nonlinear, displacement-based, geometrically-exact composite beam model (GEBM), capturing the structural dynamics, and unsteady vortex lattice method (UVLM) for the aerodynamics. Both solvers and additional methods used in this work are presented in this section.

2.1 Structural Dynamics Solver

The primary structure of the aircraft is represented by geometrically nonlinear composite beams discretized in quadratic (3-node) finite elements [10, 11] and parametrized by nodal displacements and rotations, denoted by $\boldsymbol{\eta}$ within a body-attached FoR B. These beams are modelled by the GEBM which is a geometrically nonlinear formulation with nonlinear relationships for velocity and displacement kinematics whilst maintaining linear constitutive relations. Moreover, it accounts for follower forces by expressing them in a local structural frame of reference (FoR) S. The different FoRs are illustrated in Fig. 1 with the S-frame moving and rotating with the structure. The transformation from the B to the S-frame is obtained from the transformation matrix $\boldsymbol{\mathcal{R}}^{SB}$ using Cartesian rotation vectors associated with each individual beam node.

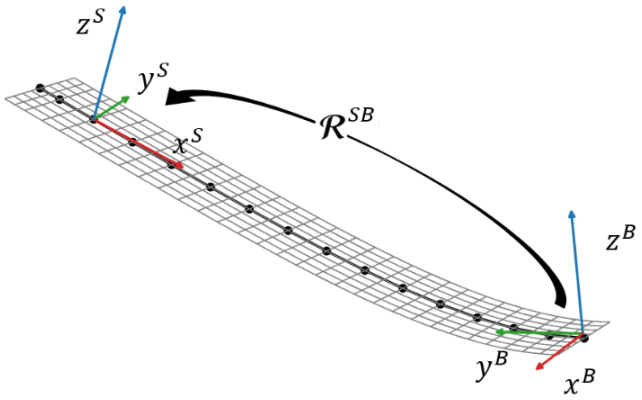

Figure 1: Illustration of the frames of reference as well as the structural and aerodynamic model of a rectangular wing.

Finally, we apply Hamilton's principle to obtain the beam dynamics whose nonlinear form is [12]

$$\boldsymbol{\mathcal{M}}(\boldsymbol{\eta})\ddot{\boldsymbol{\eta}} + \boldsymbol{\mathcal{N}}_{\text{gyr}}(\boldsymbol{\eta}, \dot{\boldsymbol{\eta}}) + \boldsymbol{\mathcal{N}}_{\text{stiff}}(\boldsymbol{\eta}) = \boldsymbol{\mathcal{N}}_{\text{ext}}(\boldsymbol{\eta}, \dot{\boldsymbol{\eta}}) \tag{1}$$

with the mass matrix $\boldsymbol{\mathcal{M}}$ and gyroscopic, stiffness, and external generalised forces $\boldsymbol{\mathcal{N}}$. Both the inertial and elastic forces are nonlinear in Eq. 1 which is solved iteratively with a Newton-Raphson scheme, while an explicit, incrementally formulated Newmark-β scheme [13] is used for the time integration.

2.2 Unsteady Aerodynamic Solver

The GEBM is strongly coupled at each time step with the UVLM as an aerodynamic solver, which is based on potential flow and thin wing theory. The UVLM predicts unsteady aerodynamic loads for three-dimensional low-speed and attached flow over thin lifting surfaces [14]. These surfaces are modelled as a lattice of quadrilateral panels whose corner points are aggregated into a column matrix $\boldsymbol{\zeta}(t)$. Each panel is associated with a bound vortex ring (index b) with a circulation, denoted by $\boldsymbol{\Gamma}_{\text{b}}$. Another grid of unbound vortex rings captures the wake (index w), which is formed due to vortex shedding generated to satisfy the Kutta-Joukowski condition at the trailing edge and the Kelvin theorem [15]. Several wake convection schemes with different fidelities to capture the shape of the wake exist. While for steady aeroelastic computations, the *horseshoe wake* is a sufficient approach, we need for unsteady computations the *convected (free) wake scheme* or *convected (prescribed) wake scheme* in which the vortex rings convect with the background flow information, which are more precisely the freestream velocity and atmospheric disturbances.

Once the geometry is established and the singularity elements are positioned on both the lifting surface and wake panels, the induced velocity field at an arbitrary point in space $\boldsymbol{r}$ can be computed from

$$\boldsymbol{u}(\boldsymbol{r}, t) = \boldsymbol{\mathcal{A}}_b(\boldsymbol{r}, \boldsymbol{\zeta}(t))\boldsymbol{\Gamma}_{\boldsymbol{b}}(t) + \boldsymbol{\mathcal{A}}_w(\boldsymbol{r}, \boldsymbol{\zeta}(t))\boldsymbol{\Gamma}_{\boldsymbol{w}}(t) \tag{2}$$

with the aerodynamic influence coefficient (AIC) matrices $\boldsymbol{\mathcal{A}}_b$ and $\boldsymbol{\mathcal{A}}_w$. The AICs contain the normal velocity component $\boldsymbol{u}(\boldsymbol{r}_{ij}, t) \cdot \boldsymbol{n}_j$ on a collocation point, located at the center of panel j with its normal vector $\boldsymbol{n}_j$, induced by the vortex ring placed on panel i, where $\boldsymbol{u}(\boldsymbol{r}_{ij}, t)$ is calculated by Biot-Savart's law. After enforcing the non-penetrating boundary condition on each collocation point j, considering any external velocities (freestream velocity $\boldsymbol{U}_\infty$ and gust velocities $\boldsymbol{w}_g$), we obtain a linear set of equations $\boldsymbol{\mathcal{A}}_l\boldsymbol{\Gamma}_{\boldsymbol{l}} = -\boldsymbol{\mathcal{B}}_l$. Here, $\boldsymbol{\mathcal{A}}_l$ is the AIC matrix,

and the boundary conditions are given by $(\boldsymbol{U}_\infty + \boldsymbol{U}_{ext}) \cdot \boldsymbol{n}$. The right hand side. The bound b and wake w vertices are combined using the subindex l, denoting the lifting surface. The solution gives the circulation strengths $\boldsymbol{\Gamma}_b$ and $\boldsymbol{\Gamma}_w$. For symmetric models, we can enforce equal circulation of the symmetric surfaces 1 and 2 with $\boldsymbol{\Gamma}_{l_1} = \boldsymbol{\Gamma}_{l_2}$. Then the linear set of equation is reduced to half its size, i.e. $(\boldsymbol{\mathcal{A}}_{l_{11}} + \boldsymbol{\mathcal{A}}_{l_{12}})\boldsymbol{\Gamma}_{1_1} = -\boldsymbol{\mathcal{B}}_{l_1}$. The lattice grid coordinates of the second surface and wake, $\boldsymbol{\zeta}_{b_2}$ and $\boldsymbol{\zeta}_{w_2}$ respectively, which are needed to compute $\boldsymbol{\mathcal{A}}_{l_{12}}$ and the *free wake* convection scheme can efficiently be deduced from its symmetric and known counterpart, namely $\boldsymbol{\zeta}_{b_1}$ and $\boldsymbol{\zeta}_{w_1}$.

2.2.1 Aerodynamic Force Computations and Correction

We compute the resulting aerodynamic forces from the circulation strengths $\boldsymbol{\Gamma}_l$. Vortex rings induce a quasi-stationary force that takes into account the suction effect of the leading edge and can be calculated at each vortex segment centre using Joukowsky's theorem. The unsteady forces are obtained at the panel center of each vortex ring following Bernoulli's principle and incorporate the additional mass effect [16]. Both force contributions are then linearly interpolated to the corners of the vortex rings $\boldsymbol{\zeta}$. These aerodynamic forces are then mapped onto the structural grid by simply summing the aerodynamic forces of all chordwise nodes at the ith spanwise structural node, which can be done because of the coincident structural and aerodynamic grids in a spanwise direction. The moments are similarly calculated by summing the moments acting on the i-th structural node generated by the corresponding aerodynamic forces by considering the lever arm between vortex ring corners $\boldsymbol{\zeta}$ and structural nodes $\boldsymbol{\xi}$.

Finally, adjustment of the lift curve slopes, including thickness or Reynolds number effects, and static lift efficiency at very high angles of attack near the onset of stall, is done with the sectional force correction method presented and validated in Ref. [17]. This correction is applied sequentially on the forces $\boldsymbol{f}_i^B$ and moments $\boldsymbol{m}_i^B$ of each structural node i by first, computing the effective sectional angle of attack while considering complex dynamics and large deformations, and second, using 2D airfoil polar data to determine the forces and moments at this given angle of attack. If only the lift curve slope is corrected, the resulting sectional forces and moments can also just be multiplied by a user-specified factor. This correction is applied within the Fluid-Structure Interaction (FSI) loop before feeding the forces $\boldsymbol{f}_i^B$ and moments $\boldsymbol{m}_i^B$ to the structural subsystem.

2.2.2 Wake Dynamics

The wake shedding at the trailing edge is determined by the conservation of circulation on ideal fluids. This is described by Kelvin's theorem, which states that the flow circulation around a closed curve does not change with time. This is satisfied here by the detachment of the first wake panel with an instantaneous circulation equal and opposite to that of the bound trailing edge panel [18, Chapter 2.3]. The trailing panels then convect downstream with the flow following Helmholtz's laws of vorticity [18, Chapter 2.9]. This convection can be tracked for each point of the wake grid $\boldsymbol{x}$ by

$$\boldsymbol{x}(t) = \boldsymbol{x}_0 + \int_0^t \boldsymbol{u}(\boldsymbol{x}(s), s)ds, \tag{3}$$

where $\boldsymbol{x}_0$ is the initial position and $\boldsymbol{u}$ is the flow velocity that includes the upstream undisturbed $\boldsymbol{U}_\infty$, the vortex-induced velocities, and atmospheric disturbances $\boldsymbol{w}_g$. This leads to an accurate computation of the wake, the axial induction and the aerodynamic forces and is the previously mentioned *free wake* model. However, the flow velocity can also be approximated by the reference velocity for efficiency reasons and is referred to as *prescribed wake*. This *prescribed wake*

though cannot capture wake-roll up effects and interference effects between different wakes as well wake and surfaces caused by the induced velocity of the vortex ring panels of those with given circulation. In some cases, as we will later see, these might or might not be negligible.

In an Arbitrary Lagrangian-Eulerian description, beneficial for moving FoRs, this wake surface is described by two curvilinear coordinates ν and ζ along the spanwise and streamwise directions. Convection of circulation only occurs along the ζ coordinate for each value of the streakline ν according to

$$\frac{\Gamma_{\zeta}^{t+1} - \Gamma_{\zeta}^{t}}{\Delta t} + u_r \frac{\Gamma_{\zeta}^{t} - \Gamma_{\zeta-1}^{t}}{\Delta \zeta} = 0, \tag{4}$$

using a first-order upwind discretization. In this equation, $\Delta\zeta$ is the vortex size in the streamwise direction, and u_r is the relative flow-solid velocity. Panel methods commonly use a Courant– Friedrichs–Lewy number $CFL \coloneqq u_r \Delta t / \Delta\zeta$ of one [18]. This simplifies the wake convection to a movement of values from one discretization element to the following, i.e. $\Gamma_{\zeta}^{t+1} = \Gamma_{\zeta-1}^{t}$. When the wake vortex rings convect, a gap between the trailing edge and the first wake node is generated. This gap is filled with a new segment parallel to the streamwise direction and the relative solid-fluid velocity, ensuring the Kutta-Joukowski condition at the trailing edge and the Kelvin theorem [15].

The formulation of the UVLM in the discrete-time domain inherently connects time integration with wake shedding. Specifically, the chordwise size of each newly shed wake vortex ring row correlates directly with the time step, establishing a connection between spatial and temporal discretization with the fixed timestep $\Delta t = \frac{c}{M \cdot U_\infty}$. One outcome of this is that a finer discretization with M panels in the chord direction requires a smaller time step. This results in more panels in the chord direction for the same physical length of the wake. Furthermore, with a fixed time step but different-sized lifting surfaces, as is the case in this work with the simultaneous simulation of the gust vanes and the Delft-Pazy wing, it is important to adjust the chordwise discretization of these surfaces so that the condition $CFL = 1$ is satisfied for all surfaces.

2.3 Linearization Process

We continue with the description of the linearization of the nonlinear aeroelastic system. This linearization is performed individually for the UVLM and GEBM and around the nonlinear aeroelastic equilibrium of the system denoted by the subscript $(\cdot)_0$, which is computed with the previously presented nonlinear solver. At this equilibrium, both structural velocities and accelerations are zero, i.e. $\ddot{\boldsymbol{\eta}}_0$ and $\dot{\boldsymbol{\eta}}_0$. In addition, the external forces must be in balance with the stiffness and gyroscopic forces, i.e. $\boldsymbol{N}_{gyr}(\boldsymbol{\eta}, \dot{\boldsymbol{\eta}}) + \boldsymbol{N}_{stiff}(\boldsymbol{\eta}) = \boldsymbol{N}_{ext}(\boldsymbol{\eta}, \dot{\boldsymbol{\eta}})$ from which we can derive the tangential damping and stiffness matrices, denoted by $\boldsymbol{\mathcal{C}}$ and $\boldsymbol{\mathcal{K}}$ respectively. With these conditions for the equilibrium state, we can perturbate the GEBM model from Eq. 1 assuming small amplitudes, resulting in the perturbation equations [19]

$$\boldsymbol{\mathcal{M}}(\boldsymbol{\eta}_0)\Delta\ddot{\boldsymbol{\eta}} + \boldsymbol{\mathcal{C}}(\boldsymbol{\eta}_0, \dot{\boldsymbol{\eta}}_0)\Delta\dot{\boldsymbol{\eta}} + \boldsymbol{\mathcal{K}}(\boldsymbol{\eta}_0, \dot{\boldsymbol{\eta}}_0)\Delta\boldsymbol{\eta} = \Delta\boldsymbol{\mathcal{N}}_{\text{ext}}(\Delta\boldsymbol{\eta}, \Delta\dot{\boldsymbol{\eta}})\,. \tag{5}$$

Here, $\Delta(\cdot)$ denotes small perturbations around the reference and the state variables consist of the flexible DoF deviations $\Delta\boldsymbol{\eta}_i$ for each node i, and their gradient $\Delta\dot{\boldsymbol{\eta}}_i$.

We further reduce the linear structural system by projecting it onto the modal coordinates of the deformed system and truncating it to a suitable number of modes n_q that capture the most important dynamics. More precisely, this modal projection, expressed as $\Delta\boldsymbol{\eta} = \boldsymbol{\Phi}\Delta\boldsymbol{q}$ and $\Delta\dot{\boldsymbol{\eta}} = \boldsymbol{\Phi}\Delta\dot{\boldsymbol{q}}$, is obtained by calculating $\boldsymbol{\Phi}$ from the solution of the eigenvalue problem by

inserting Eq. (5) into the above equations. The modal displacement field $\boldsymbol{q}$ and the resulting modal velocities $\dot{\boldsymbol{q}}$ then describe the structural dynamics.

Subsequently, we analytically linearize the UVLM with the assumption of constant AICs and a frozen wake shape while including steady load effects. This yields a discrete, linear time-invariant (DLTI) system in state-space, as demonstrated by Maraniello and Palacios [20]. The gust inputs which map three-dimensional velocity vectors to each vortex-ring panel, leading to a high number of inputs, have been reduced to a single gust input $\boldsymbol{w}_g$ as described in Ref. [12]. This input characterizes the vertical velocity at the foremost leading edge and maps it with the states $\boldsymbol{x}_{w_g}$ across the lattice grid points $\boldsymbol{\zeta}$. This mapping is based one a linear interpolation approach while considering a convection of this gust velocity downstream with the freestream velocity (as does any disturbance in the UVLM).

The final augmented DLTI-UVLM is written as

$$\boldsymbol{x}_a(k+1) = \boldsymbol{A}_a \boldsymbol{x}_a(k) + \boldsymbol{B}_a \boldsymbol{u}_a(k) \tag{6}$$

$$\boldsymbol{y}_a(k) = \boldsymbol{C}_a \boldsymbol{x}_a(k) + \boldsymbol{D}_a \boldsymbol{u}_a(k)\,, \tag{7}$$

with the states $\boldsymbol{x}_a(k) = \left[\Delta\boldsymbol{x}_{w_g},\, \Delta\boldsymbol{\Gamma}_b,\, \Delta\boldsymbol{\Gamma}_w,\, h\Delta\dot{\boldsymbol{\Gamma}}_b,\, \Delta\boldsymbol{\Gamma}_b(k-1)\right]$ and the output is composed of the dimensionless forces, including steady and unsteady components, at these vertices, and is written as $\boldsymbol{y}_a(k) = \Delta\boldsymbol{F}(k)$. The inputs are $\boldsymbol{u}_a(k) = \left[\Delta\boldsymbol{\zeta},\, \Delta\dot{\boldsymbol{\zeta}},\, \Delta\boldsymbol{w}_g\right]$. The integers k and h are the current discrete time step and its size. To improve readability, we omit specifying the discrete time step of an aeroelastic parameter if referring to the current time step. We capture the added mass effects with the time-derivative $\dot{\boldsymbol{\Gamma}}$, computed with second-order accuracy (thus $\Delta\boldsymbol{\Gamma}_b(k-1)$ as a state).

To couple the aerodynamic and structural dynamic systems, the aerodynamic force output $\Delta\boldsymbol{F}$ stemming from the DLTI-UVLM system in the B-frame is projected onto the structural DoF in the S-frame. These transformed forces can then be input directly into the GEBM system as forces and moments using linear mapping [19]. The GEBM system then yields the resulting grid geometries and velocities based on the subsequent node displacements and velocities, which then serve as inputs to the DLTI UVLM system.

The resulting linearized coupled aeroelastic system

$$\begin{aligned}\boldsymbol{x}_{ae}(k+1) &= \boldsymbol{A}_{ae}\boldsymbol{x}_{ae}(k) + \boldsymbol{B}_{ae}\boldsymbol{u}_{ae}(k)\\ \boldsymbol{y}_{ae}(k) &= \boldsymbol{C}_{ae}\boldsymbol{x}_{ae}(k) + \boldsymbol{D}_{ae}\boldsymbol{u}_{ae}(k)\,,\end{aligned} \tag{8}$$

has now the input $\boldsymbol{u}_{ae}(k) = \Delta\boldsymbol{w_g}$, and the following states and outputs for the linear full-order model (FOM) system:

$$\boldsymbol{x}_{ae}(k) = \left[\Delta\boldsymbol{x}_{w_g},\, \Delta\boldsymbol{\Gamma}_b,\, \Delta\boldsymbol{\Gamma}_w,\, h\Delta\dot{\boldsymbol{\Gamma}}_b,\, \Delta\boldsymbol{\Gamma}_b(k-1),\, \Delta\boldsymbol{q},\, \Delta\dot{\boldsymbol{q}}\right]$$

$$\boldsymbol{y}_{ae}(k) = \left[\,\Delta\boldsymbol{\mathcal{N}}, \Delta\boldsymbol{\eta},\, \Delta\dot{\boldsymbol{\eta}}\right]\,.$$

Here, $\Delta\boldsymbol{\mathcal{N}}$ denotes the structural forces and moments.

3 DELFT-PAZY WING DESIGN, EXPERIMENTS AND COMPUTATIONAL MODEL

3.1 Delft-Pazy Wing Design and Ground Vibration Test

The Delft-Pazy wing design is mostly identical to the Pazy wing that is described in detail in Ref. [2]. This unswept and untapered wing has a chord length of $c = 100$ mm and a span width of $s = 550$ mm. The main difference between the original Pazy wing and the Delft-Pazy wing is a reduced thickness of the inner spar plate made from aluminium, which is 1.5 mm for the Delft-Pazy wing instead of 2.25 mm. This modification has been implemented to produce comparably large deformations to those observed on the Pazy wing at the Technion in a low-speed wind tunnel facility at TU Delft. Furthermore, the outer surface of the Delft-Pazy wing is covered with non-reflective black paint to facilitate optical flow field measurements in the wind tunnel. On this coating, a pattern of white circular reflective markers is applied for tracking the structural motion of the wing, as shown in Fig. 2.

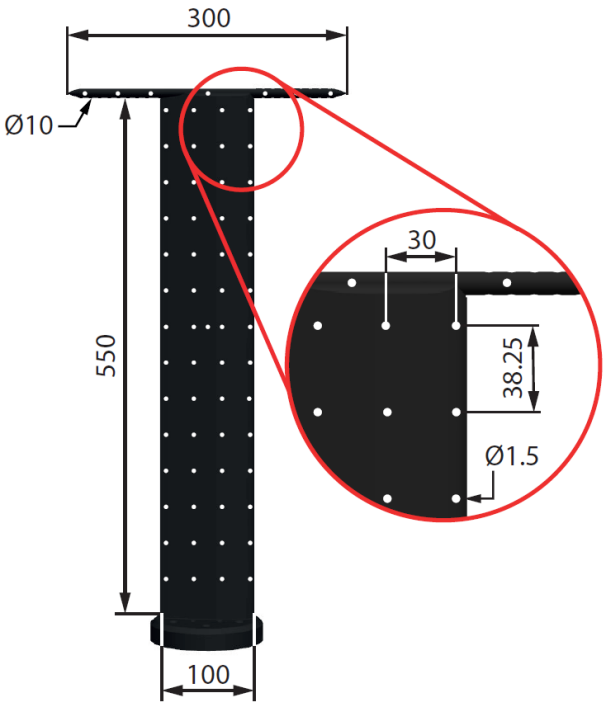

Figure 2: Sketch of the Delft-Pazy wing. Dimensions are in mm.

To characterize the structural behavior of the Delft-Pazy wing, a ground vibration test (GVT) was performed prior to the wind tunnel experiment. The GVT is performed using a modal hammer and a laser scanning vibrometer. More details about the wing design and the GVT are provided in Ref. [5]. The GVT results provide the first five experimental mode shapes and frequencies included in the later discussed Tab. 2.

3.2 Wind Tunnel Experiment

The wind tunnel experiment was performed at the Open Jet Facility (OJF) at TU Delft. The OJF is a closed-loop, open test section wind tunnel with an octagonal outlet spanning 2.85 m by 2.85 m, which was operated at a freestream velocity of 18.3 m/s. A photograph of the wind tunnel setup with an indication of the relevant components is shown in Fig. 3.

Upstream of the wing, at a distance of approximately 1.5 m from the Delft-Pazy wing that is placed at the center of the test section, are the two vertical gust vanes which are operated in a continuous sinusoidal pitching motion during the tests. The Delft-Pazy wing itself is mounted

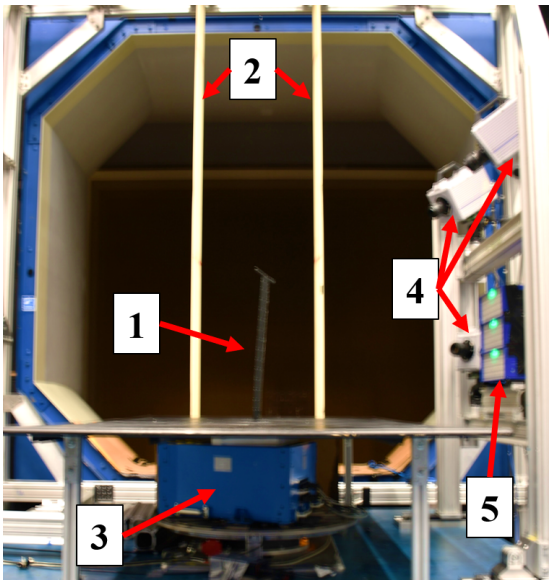

Figure 3: Photo of the wind tunnel setup in the OJF, looking upstream. 1: Delft-Pazy wing, 2: gust generator vanes, 3: six-component balance, 4: 3x high speed cameras, 5: 3x LED illumination units.

vertically on a six-component balance. On the right side in the photo in Fig. 3 is the optical measurement setup. The main objective of the wind tunnel experiment was the development of an aeroelastic characterization approach that describes the unsteady loads acting on the wing based on non-intrusive measurements with this optical setup, as described in detail in Ref. [5]. For the purpose of this study, the focus is placed on the structural response of the wing to the periodic gust excitation, therefore the measurement of both of these is described in the following.

The structural response of the wing is measured experimentally by tracking the markers on the surface with the same optical measurement system that is conventionally only used for flow field measurements in an integrated measurement approach [21]. Due to limitations of the measurement volume size of this system, several measurements of the structural response in terms of the marker displacements at different locations of the wing were combined into one data set and subsequently analyzed in a phase-averaged approach. In this approach, a sinusoidal fit was performed for the periodic displacement per marker and afterwards, the wing shape was reconstructed to best fit these measurements based on a polynomial fit of the spanwise central axis of the wing. Torsional deformations were analyzed and considered small enough in the experiments to be neglected for the considered test cases. The wing deformation is thus described solely in terms of the out-of-plane bending and can therefore be summarized in terms of a mean tip deflection w, a dynamic tip deflection amplitude $\hat{w}$, and a phase lag Φ of the dynamic wing motion with respect to the incoming gust (see Tab. 1).

Table 1: Overview of the dynamic wind tunnel test conditions and wing deflection results.

test case	angle of attack α	static tip deflection w/s	gust frequency f_g	tip deflection amplitude $\hat{w}/s$	phase shift to incoming gust Φ	measured gust amplitude A_g
1	5 deg	8.5%	5.7 Hz	1.8%	−171 deg	0.81 m/s
2	10 deg	15.9%	3.2 Hz	8.2%	+99 deg	0.65 m/s

The phase and amplitude of the incoming gust are determined experimentally based on the

phase-averaged flow field measurements in the wind tunnel. This is achieved by analyzing the variation in the transversal velocity component upstream of the wing at $x = -0.75c$, see Fig. 4. This location has been selected because it is near the upstream edge of the measurement volume, where flow field information is available. Measurements further upstream would be desirable to further reduce the effect of the presence of the wing on the gust velocity measurement but could not be realized in the experimental campaign. At the selected location, the transversal velocity component exhibits a nearly ideal sinusoidal behavior, which permits the quantification of the phase and angle and gust amplitude as given in Tab. 1. More details about the flow field measurements and data processing can be found in Ref. [5].

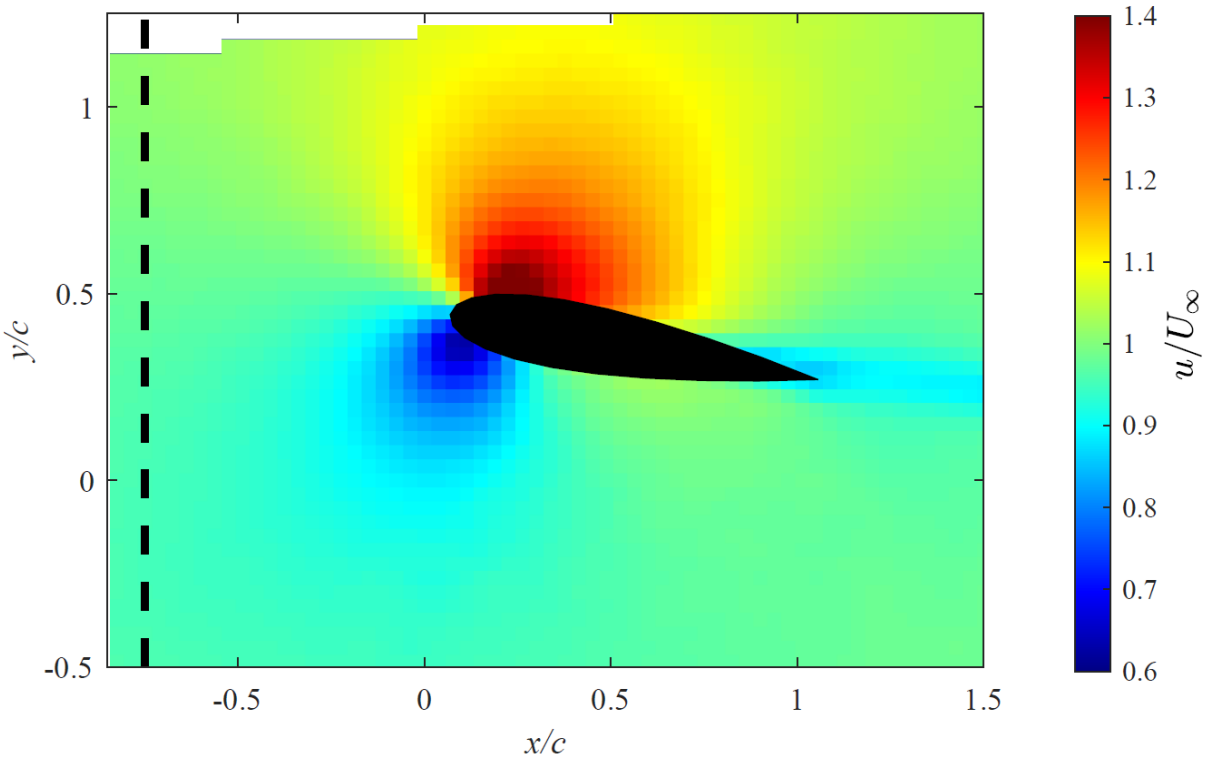

Figure 4: Measurement of the flow field at mid-span during the upstroke of the wing motion in test case 2. The upstream location where the gust velocity is extracted is indicated with the dashed line. The origin of the coordinate system is at the leading edge of the undeformed wing.

3.3 Computational Model Implementation

An implementation of the Delft-Pazy model is implemented into SHARPy, where the aerodynamic lifting surfaces are modeled using a flat plate of vortex panels, while the primary structure is depicted by a one-dimensional beam. The main sectional structural stiffness and mass properties along the wing are shown in Fig 5 and are derived from the work of Riso et al [22]. Similar methodologies have been employed previously to construct the equivalent beam model for the Technion Pazy using the Enhanced FEM2Stick (EF2S) framework, as described in Ref. [23]. This EF2S framework assumes infinite shear stiffness and that is employed in this work as well.

The modal frequencies of SHARPy's Delft-Pazy model under unloaded conditions are compared with the frequencies obtained from the GVT as well as the FEM Nastran model used in the EF2S to create the beam model. The results are shown in Tab. 2. Between the FEM model and SHARPy we observe an excellent agreement, where the maximum relative error is just above one percent for the first five modes. The second torsional mode which, however, has a very high frequency and is less crucial for the aeroelastic dynamics, differs by $6.14\,\%$. The

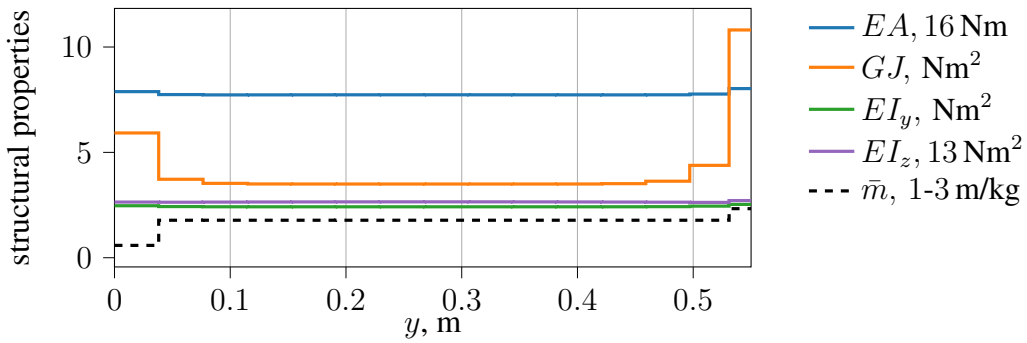

Figure 5: Sectional structural stiffness and mass distribution of the beam model.

Table 2: Comparison of the modal frequencies.

mode	description	f_{GVT}	f_{FEM}	f_{SHARPy}	$\epsilon(f_{\text{GVT}}, f_{\text{FEM}})$	$\epsilon(f_{\text{FEM}}, f_{\text{SHARPy}})$
1	OOP1	3.21 Hz	3.43 Hz	3.45 Hz	6.83 %	0.58 %
2	OOP2	22.47 Hz	22.81 Hz	23.12 Hz	1.51 %	1.36 %
3	T1	29.49 Hz	31.29 Hz	31.26 Hz	6.10 %	−0.10 %
4	OOP3	64.99 Hz	65.85 Hz	66.54 Hz	1.32 %	1.05 %
5	IP1	n.a.	106.29 Hz	107.40 Hz	n.a.	1.04 %
6	T2	119.70 Hz	118.25 Hz	125.50 Hz	−1.21 %	6.13 %

frequencies of the actual Delft-Pazy wing measured in the GVT differ slightly from the FEM model (and thus SHARPy) with the relative deviation defined as $\epsilon(f_1, f_2) = (f_2 - f_1)/f_2$ being in reasonable ranges for GVT measurements [5]. Note that the in-plane bending mode could not be captured with the selected GVT setup but have been important in the nonlinear flutter solutions of Goizueta et al [24].

4 GUST-INDUCED WING DEFORMATION PREDICTION

The capabilities of the nonlinear aeroelastic solver are excercised in this section to compute the steady and gust-induced dynamic deformations of the Delft-Pazy with the experimental results serving as a reference. The cantilever wing is simulated with a symmetry condition applied at the root. The beam is discretized into 30 elements, resulting in 61 spanwise vortex ring panels on the lifting surface. In chordwise direction, 8 vortex ring panels are employed. For the steady results, horseshoe vertices model the wake. For the dynamic computations, a wake length of $20c$ is chosen and the prescribed gust convection model is used as the deformation difference to the results using a free wake model are negligibly small ($< 0.2\,\%$). This discretization shows good convergence criteria for both the structural dynamics and aerodynamics.

4.1 Steady Results

We start with computing the steady deformation of the Delft-Pazy wing under the given wind tunnel freestream conditions with a Reynolds number of $Re = 122,000$. The lift curve of the NACA0018 airfoil for this Reynolds number is obtained with XFOIL and shown in Fig. 6. At lower angles of attack α between -1.5 deg and 2.3 deg, this lift curve has a slope of $1.25 \cdot 2\pi$. At $\alpha = 2.3$ deg the lift curve features a small kink and continues with a higher slope. From $\alpha = 5.4$ deg onwards, flow separation becomes increasingly important.

These conditions must be incorporated in the nonlinear aeroelastic simulation to expect realistic prediction of the aerodynamic forces. This can be achieved with either a constant correction of the lift curve slope c_{l_α} by a factor of 1.25 for lower angles of attack or the described sectional

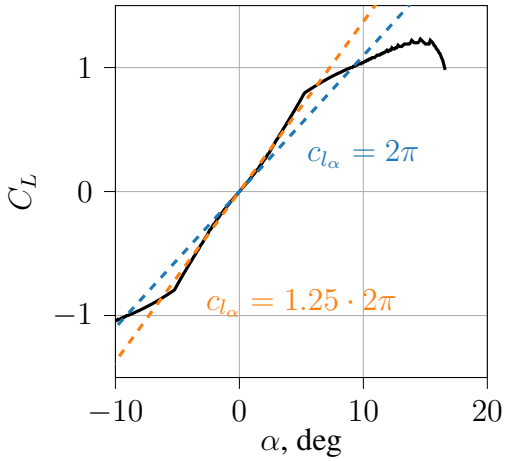

Figure 6: Lift curve of the NACA0018 airfoil computed with XFOIL for $Re = 122,000$.

force correction, using this lift curve as an input. The resulting wing deformations are illustrated in Fig. 7 and compared with the experimental deformations for the investigated angles of attack of $\alpha = 5\,\text{deg}$ and $\alpha = 10\,\text{deg}$.

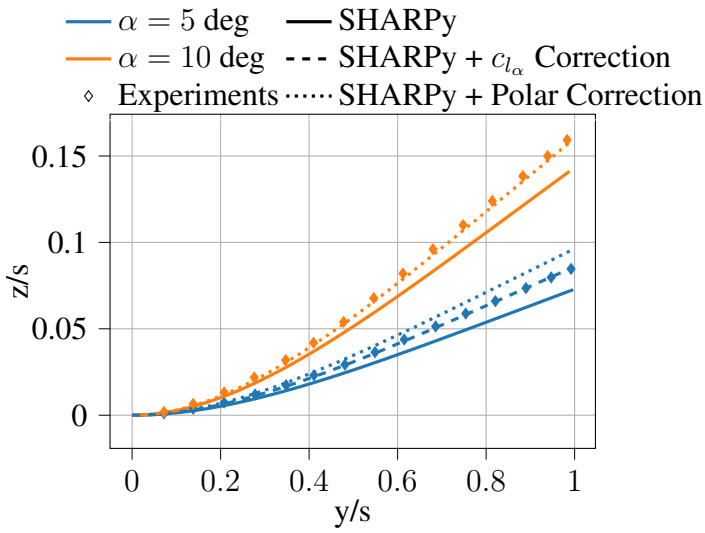

Figure 7: Steady wing deformation prediction of the Delft-Pazy wing.

Without the force correction, the wing deformation is underestimated in the nonlinear aeroelastic simulation for both angles of attack. The tip deformation in that case deviates by $-14.19\,\%$ and $-11.40\,\%$ for $\alpha = 5\,\text{deg}$ and $\alpha = 10\,\text{deg}$, respectively. The c_{l_α} correction results in an almost matching deformation prediction for $\alpha = 5\,\text{deg}$ but the polar corrections result in an overestimation. Both resulting in reduced wing tip displacement errors of $0.96\,\%$ and $13.05\,\%$. These different performances likely stem from deviations of the sectional lift curve obtained from XFoil and the actual experimental one which is not available. For $\alpha = 10\,\text{deg}$, the polar correction reduces the error in wingtip displacement to $-1.38\,\%$.

4.2 Dynamic Results

We continue with presenting the dynamic gust response prediction of the Delft-Pazy wing for the two conditions summarized in Table 1. The same force corrections as in the steady computations are used for each case. The measured gust input from the experiments is used as a

frozen gust input to the nonlinear aeroelastic solver in the form of a time series. The solver then maps the gust velocities to the vortex ring collocation points and wake lattice grid points for the aerodynamic solution. The gust response is then run for several timesteps until the wing deformation excitation converges to a uniform oscillation. One period of these converged results and the experimental deformation measurements are shown in Fig. 8 for both cases at spanwise positions of $y/s = 0.9$. The displayed gust velocity corresponds to the gust velocity at the quarter chord of the wing.

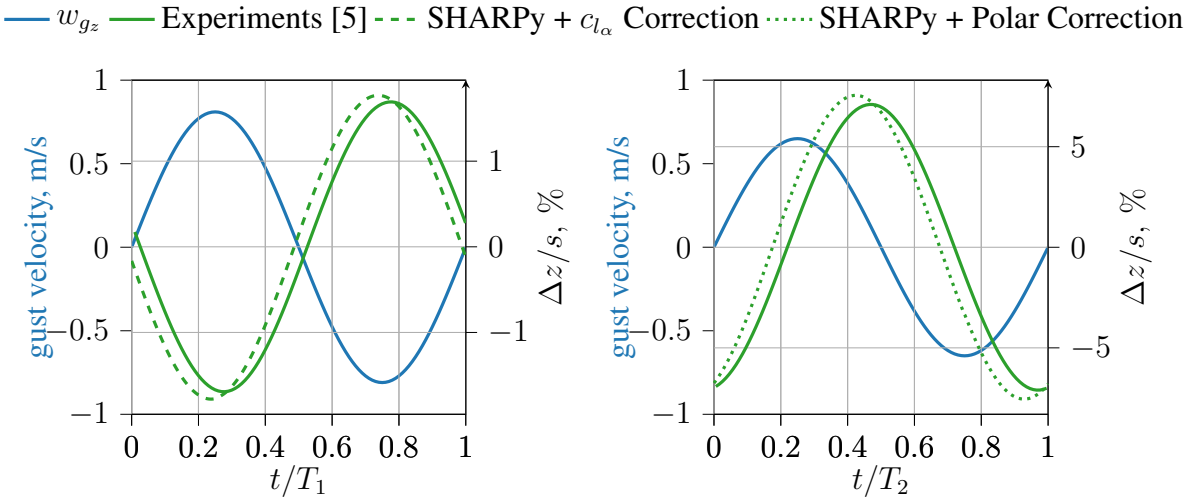

(a) Case 1.

(b) Case 2.

Figure 8: Increments of the dynamic vertical wing deflection from the mean value at $y/s = 0.9$.

For case 1, the experimental mean deflection is $z/s = 0.085$ and the amplitude $\Delta z/s = 0.018$. Without any sectional force correction applied, both mean and amplitude are significantly underestimated by the nonlinear aeroelastic solver, as expected from the observations made in the previous sections. The polar correction results in a mean error of only $-1.85\,\%$ but the amplitude deviates by almost $10\,\%$. The c_{l_α} correction, shown in Fig. 8(a), leads to a small overestimation of the mean and amplitude value by $5.73\,\%$ and $1.48\,\%$, respectively.

For case 2, a mean deflection of $z/s = 0.159$ has been measured for the Delft-Pazy wing. The amplitude is $\Delta z/s = 0.082$ and higher than in the first case due to a gust frequency being closer to the modal frequency corresponding with the first wing root bending moment. The computational results are significantly improved with the polar corrections regarding the mean and amplitude, namely from $-14.09\,\%$ to $-2.38\,\%$ and $-23.50\,\%$ to $1.80\,\%$.

The sectional force corrections applied improve the dynamic results significantly as well while different trends have been observed from the steady results. We would like to emphasize here that the sectional force corrections are quasi-steady corrections while with reduced frequencies of $k = 0.55$ and $k = 0.98$ for case 1 and 2 respectively, unsteady aerodynamic characteristics are expected, even more dominant in case 1. These discrepancies may affect the deviations observed from the dynamic prediction and unsteady data might be necessary to improve unsteady computations at low Reynolds number with potential flow methods. Another reason, apart from the fidelity applied, can be faulty measurement of the gust input which will be examined further in the following section.

The experiments in Ref. [5] have also concluded a phase shift Φ between the gust, indicated by the blue curve in Fig. 8, arriving at the wing and the observed deformations. Reason being for

these phase shifts is the response of the harmonically forced dynamic system to the different gust frequencies. The differences between the computationally and experimentally observed phase shifts are $\Delta\Phi = -21.5$ deg for case 1 and $\Delta\Phi = -32.1$ deg for case 2. The phase shift is with less than $0.2\,\%$ barely affected by the polar and c_{l_α} corrections for case 1. The polar corrections applied on the aerodynamic predictions for case 2 increase the magnitude of the phase shift difference only by $1.11\,\%$.

5 GUST VANE MODELLING

Instead of using the measured gust as a frozen gust field input, the wake modelling featured by the UVLM enables us to model the gust generated by the gust vanes with the *free wake* model. To do so, we model the gust vanes, as illustrated in Fig. 9, as lifting surfaces and deflect them by pre-defined inputs $\delta(t)$, matching the experimental operation conditions, namely maximum gust vane deflections of ± 5 deg at frequencies of 5.7 Hz and 3.2 Hz, for case 1 and 2, respectively. The shed vortex ring panels from these vanes convect downstream and induce velocities on the wing, equivalent to the gust input. The difference to the previously defined gust input is that the singularities distributed on the Delft-Pazy wing and its wake interact with the gust through these induced velocities and their effect on the wake convection as expressed in Eq. (3). The methods employed do not capture the dissipation of the wake from the gust vanes, whose impact is assessed here.

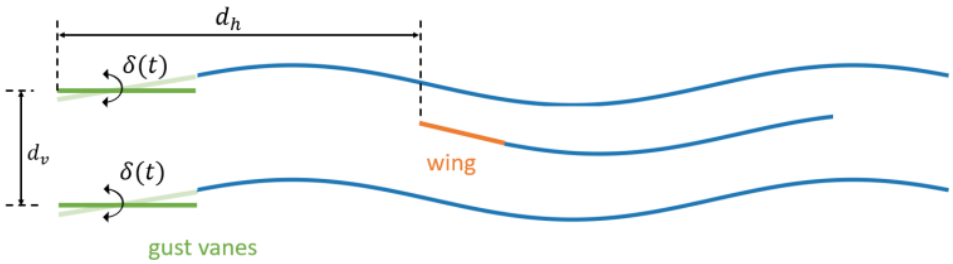

Figure 9: 2D illustration of the gust vane modelling simultaneously with the Delft-Pazy.

These interferences between gust and wing/aircraft are neglected using the frozen turbulence model, or Taylor's hypothesis, which is valid when the velocity of the aircraft flying through it is much larger than the rate of change of turbulent velocities [25]. In this section, we intend to explore the effect of the frozen turbulence assumption on the gust prediction. In addition, we investigate the local influence of the present wing on the gust as this might have caused erroneous gust measurements in the experiment.

The size of chordwise panels of the lattice grid of the gust vanes is matched to the discretisation of the wing to ensure $CFL = 1$ for the wake shedding at all surfaces. If the vanes are too coarsely discretized, resulting in a CFL number greater than one, the wake convection has been shown to not reflect the actual physical behaviors accurately. The gust vanes' half-wing span is designed to be ten times larger than that of the Delft-Pazy, preserving two-dimensional flow conditions near the center. The spanwise discretization utilizes 40 vortex ring panels to achieve a stable and converged velocity field. To avoid numerical instabilities caused by the interaction between the wakes of the two structures, the length of the wake behind the vanes is set to $50c$, significantly longer than the Delft-Pazy's wake length of $20c$.

5.1 Local Influence of Present Wing on Gust Measurements

We start with simulating the gust vanes without the Delft-Pazy wing and compute the induced velocities using Eq.(2) upstream of the wing position, more precisely at $x/c = -0.75$, matching

the experimental gust measurement point. The resulting converged induced velocity oscillations at this location are higher with $1.0\,$m/s than measured in the experiments ($0.81\,$m/s) for case 1 and $0.78\,$m/s instead of $0.65\,$m/s for case 2. This observed overprediction aligns with the comparison of the induced-gust velocities obtained from a gust vane simulation using the UVLM [7] with the CFD simulations obtained in Ref. [8].

The likely reason for these discrepancies is the absence of dissipation modeling in the potential flow model, which may be compounded by wind tunnel effects. The gust vanes are still useful for exploring interference effects, particularly focusing on gust measurements obtained within the Delft-Pazy experiments. To further investigate this interference, we simulate the gust vanes simultaneously with the current Delft-Pazy model. After achieving a convergent dynamic response, the induced velocities at the position of the gust measurements ($x/c = -0.75$) are extracted. We can decompose the contribution of the individual sources to the induced velocity and thus identify the individual influence of the shed vortices of the gust vanes and the wing vortices on the overall velocity field.

The resulting amplitude of the induced velocity oscillations are presented in Fig. 10 for both cases, once considering only the vortices of the gust vanes and their wakes, and second with all vortex ring panels considered. Hence, the difference between the blue and orange curves stems from the local influence of the wing itself. The leading edge of the wing is at $x/c = 0$ and upstream of the wing we can observe an exponential increase in the induced-velocity amplitude because of the decreasing distance to the vortex ring panels. At the gust measurement point, the interference effect for both cases is still significant, indicating an overprediction of the gust amplitude by $29.34\,\%$ for case 1 and $24.1\,\%$ for case 2. For case 1, the local wing influence becomes negligible from $x/c < -2.7$ with a difference less than $0.1\,\%$. For case 2, we reach this difference further upstream at $x/c = 3.5$, indicating a frequency dependency.

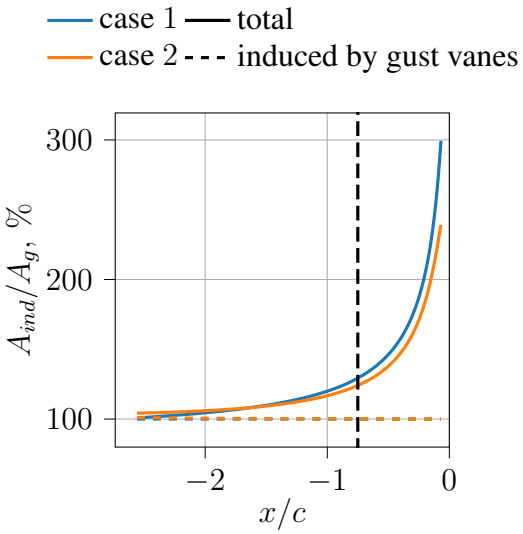

Figure 10: Streamwise variation in the amplitude of induced velocity oscillations at $z = 0$ upstream the airfoil.

In addition to the local influence of the wing, we now address the vertical stratification in the induced gust velocities because of the local distance to the gust vane wakes. This vertical stratification is neglected in the commonly used one-dimensional gust input. Fig. 11 shows the deviations in the induced gust amplitude at $x/c = -0.75$ along the vertical axis z, which is here normalized by the distance between the vanes, denoted by d_v.

As expected the induced velocities are higher close to the convecting gust vane wakes. If we compare the simulation of only the gust vanes with the combined Delft-Pazy and gust vane one, we see the effect of the wing deflecting the gust vane wakes which introduces an asymmetric vertical stratification. More precisely, the deformed wing towards the positive vertical direction causes especially the upper wake to be deflected upwards, thus causing smaller induced velocities than without these interference effects. Also, the stratification depends on the gust frequency with much higher deviations occurring for case 1 than case 2.

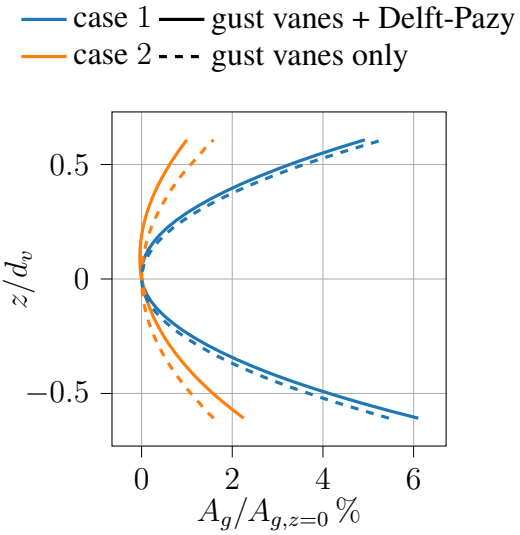

Figure 11: Vertical stratification of the relative gust velocity amplitude at $x/c = -0.75$.

We further observe oscillations in the streamwise induced velocity by the gust vanes which grow closer to the wing. However, the amplitude is less than $0.5\,\%$ of the freestream velocity since this induced velocity aligns with the flow velocity, the contribution to the effective gust angle is expected to be negligible.

5.2 Gust Modelling Effect on Deformation Prediction

After analyzing the effect of the gust vane modelling on the velocity field, we investigate next the influence of the computed structural deformations. Therefore, we extract the measured induced velocities by the gust vanes' wakes and use these velocities as a frozen gust input.

The resulting deformations of the converged oscillations are shown in Fig. 12. For both cases, the deformations obtained with the gust vane modelling and the frozen gust input match well. For case 2, these deviations are significantly lower with an error smaller than $0.05\,\%$ for both mean and amplitude. The effect on the phase shift is also negligible. For case 1, deviations in the mean deformation are only $0.42\,\%$ but the amplitude deviates by $-4.47\,\%$ and the phase becomes more affected. More notable differences are likely observed in case 1 for the different gust modelling methods because of the more dominant unsteady aerodynamic effects because of the prevailing higher gust frequency.

5.3 Note on Computational Cost

The simulations are run on a high-performance computer using an AMD EPYC™ 7742 with a clock rate of 2.25 GHz, 50 GB memory, running 8 cores in parallel. The simulation time mostly depends on the timesteps necessary to achieve converged oscillations. For frozen gust inputs, this is achieved for case 1 after 3500 timesteps while case 2 requires 4500 timesteps

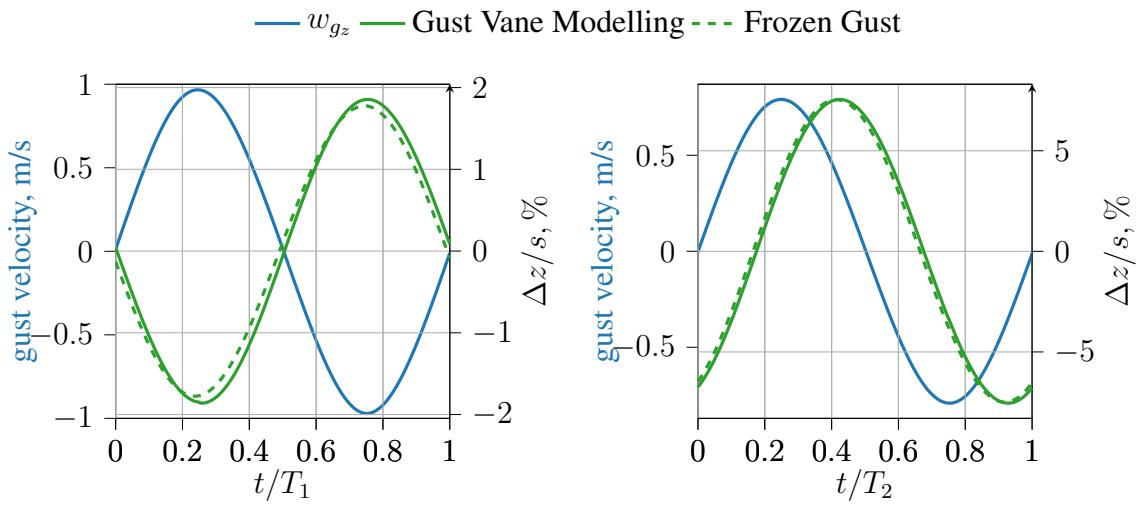

(a) Case 1.

(b) Case 2.

Figure 12: Dynamic vertical wing deflection at $y/s = 0.9$ for different gust models.

because of the higher deformations. This results in a CPU time of 221.69 and $286.30\,\mathrm{h}$ or elapsed time of $25.0\,\mathrm{h}$ and $32.1\,\mathrm{h}$ for case 1 and 2, respectively. For the gust vane simulation, the computational cost per timestep is much higher since we simulate two additional surfaces and more importantly, two more and much longer wakes. However, since the induced velocities converge quickly, i.e. less than 1000 timesteps, the computational time is comparable to the dynamic frozen gust simulations. The combined simulation of gust vanes and Delft-Pazy are clearly the most expensive computationally, taking around 7.5 times more than the frozen gust simulations.

6 ASSESSMENT OF NONLINEARITIES

This section analyses the extent of geometrical nonlinearities becoming apparent in the gust response studies for the Delft-Pazy wing. As a first test, the nonlinear aeroelastic simulations from Section 4 (including the force corrections) of the two experimental test cases are computed with the gust amplitude scaled by $1\,\%$ and $10\,\%$. The resulting converged tip displacement amplitude for both cases scale by the same numbers which indicates linear results.

To investigate this further, and to go beyond the frequencies considered in the experiments, we linearize the Delft-Pazy first around its nonlinear aeroelastic equilibriums at $\alpha_0 = 5\,\mathrm{deg}$ and $\alpha_0 = 10\,\mathrm{deg}$. Second, we linearize around the undeformed equilibriums, i.e. $\alpha_0 = 0$, to obtain a fully linear model. The simulations in this section consider a horizontally mounted wing and no gravity since the linearization and the gust assembler are only functional for this setup. Also, the force correction methods have only been implemented into the nonlinear aeroelastic solver and are thus not used here. Note that especially due to the missing polar corrections, the tip displacement amplitude is higher for these conditions than before.

The first step is to check the linearity of all three models by comparing their response to a small amplitude gust for which $1\,\%$ of the experimental gust velocities are used with the frequencies of $5.7,\mathrm{Hz}$ and $3.2\,\mathrm{Hz}$ with the nonlinear aeroelastic results. Each linear FOM is compared to the nonlinear results obtained from the same angle of attack it is linearized around. Starting with a frequency $5.7,\mathrm{Hz}$, we obtain an excellent match between nonlinear and linear results regarding the resulting tip displacement amplitudes of the converged oscillations with errors of

less than $0.5\,\%$ for the fully linear FOM and the linear FOM, linearized around its equilibrium at $\alpha_0 = 5\,\text{deg}$. Their transient response following the gust onset is captured perfectly as well. For the FOM, linearized around $\alpha_0 = 10\,\text{deg}$, the converged amplitudes deviate slightly with $1.20\,\%$. For a frequency of $3.2,\text{Hz}$, we observe for the FOM, linearized around $\alpha_0 = 10\,\text{deg}$, constant offset in the gust amplitudes by $7.77\,\%$. An amplitude deviation of $1.57\,\%$ and $-2.72\,\%$ result for the fully linear FOM and the FOM, linearized around $\alpha_0 = 5\,\text{deg}$.

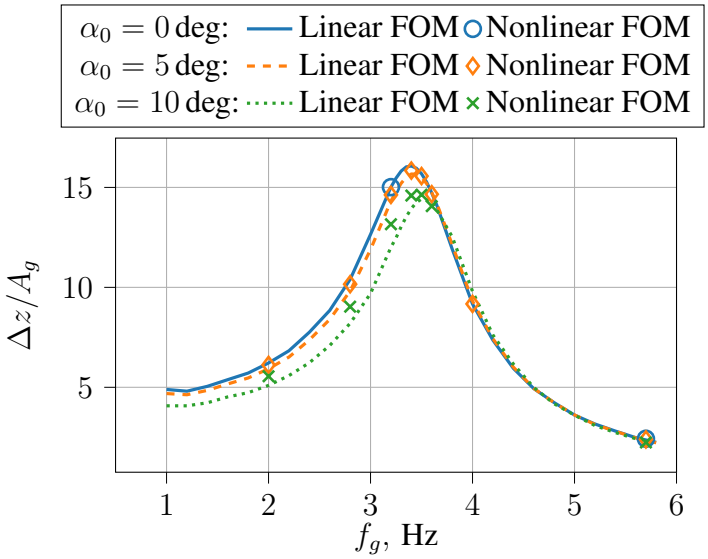

Figure 13: Wingtip displacement amplitude over various gust frequencies.

Next, we compute the expected oscillated wingtip displacement amplitudes for the different gust amplitudes for frequencies in the range from $f_g = 1\,\text{Hz}$ to $f_g = 5.8\,\text{Hz}$ using the linear FOMs. The amplitudes are normalized by the gust amplitude and are displayed in Fig. 13. The peak in the wingtip displacement amplitude is attributed to the first (OOP) bending mode. The frequency of this modes varies for the different linear FOMs as the modal frequencies shift with wing deformation. Moreover, the peak amplitude reduces with the linear FOM, which is linearized for increasing angles of attack, due to geometrical stiffening at higher deformations. Although the three linear FOMs converge to similar wingtip displacement amplitudes at higher frequencies, a noticeable difference between the FOMs is evident at frequencies lower than the first modal frequency. While for frequencies higher than this frequency, all FOMs converge to the same wingtip displacement from around $f_g = 4\,\text{Hz}$, an offset between the FOMs can be observed for decreasing frequencies.

We continue with examining the extent of geometrically nonlinear effects becoming apparent for different frequencies as there is clearly a dependency observable. Therefore, we compute with the nonlinear FOM the resulting wingtip displacement amplitudes for different combinations of gust frequencies f_g and amplitudes A_g. The results obtained with a gust amplitude of $0.65\,\text{m/s}$ are marked in Fig. 13. If we excite the Delft-Pazy wing with a sinusoidal gust in the undeformed state, the wingtip deformation amplitude obtained with the nonlinear FOM match the linear results for the frequencies of $3.2\,\text{Hz}$ and $5.7\,\text{Hz}$ with less than a deviation of $1\,\%$. However, a fully linear FOM is not sufficient in predicting the results of the moderately large steady deflections of the Delft-Pazy model.

For the linear FOMs obtained from their nonlinear aeroelastic equilibrium, we observe that close to the resonance peak the nonlinear predictions match the linear predictions well with less

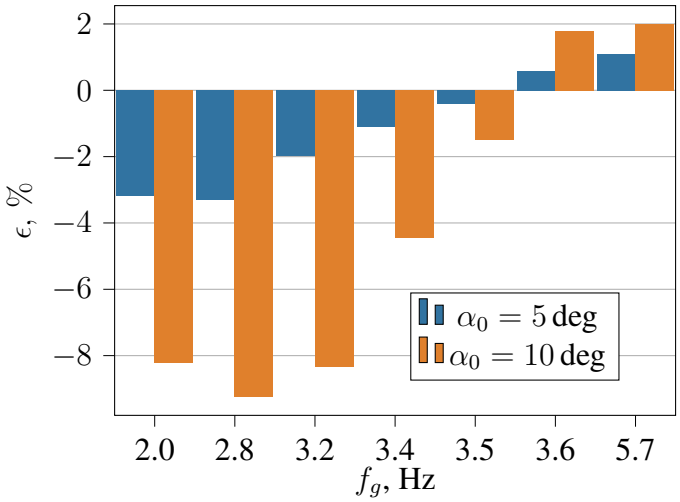

Figure 14: Deviations ϵ of the wingtip displacement amplitudes obtained with the linear and nonlinear FOM.

than one percent of deviation. But farther away, both towards lower and higher frequencies, the deviations increase as illustrated in Fig. 14. More precisely, the amplitudes at lower frequencies are underpredicted by the linear FOMs and overpredicted for higher frequencies. However, the error observed is much smaller for the FOM, linearized around the less deformed wing at $\alpha_0 = 5\,\text{deg}$. In addition, the difference in the nonlinear results for $\alpha_0 = 5\,\text{deg}$ and $\alpha_0 = 10\,\text{deg}$ indicate the presence of nonlinearities, however, rather linked to the nonlinear aeroelastic equlibrium than the gust excitation.

The question arises if these deviations can be explained with nonlinearities, especially since we have seen during the verification study of the linear FOMs, that notable deviations occur even with small gust amplitudes. Hence, we computed the wingtip displacement amplitudes of the nonlinear FOM for gust in this lower frequency range and interestingly, the relative error remains constant for lower gust amplitudes. This rather indicates an error within the linearization process for highly deformed wing shapes.

7 CONCLUDING REMARKS

This work has investigated the modelling capabilities of the nonlinear aeroelastic simulation toolbox SHARPy for the dynamic gust response of the very flexible Delft-Pazy. This wing has been experimentally tested at TU Delft with present unsteady aerodynamic flow and moderately large structural deformation. A numerical model was implemented into SHARPy.

First, we have computed for this model the steady and dynamic gust-induced deformation and compared the instantaneous structural deformations with the experimental results. For the steady case, excellent agreement was achieved by applying sectional force corrections to account for the present low Reynolds number and separation onset effects which are both not captured in potential flow models. Different corrections are needed for each angle of attack. For the dynamic case, the prediction of the deformation amplitudes also matches well with the experiments. However, more notable (but still small) deviations can be observed in the mean of the structural oscillations, especially for the first case with more dominant unsteady flow effects with an error $5.73\,\%$. These deviations can be explained by the quasi-steady force corrections methods applied on an unsteady problem but also stem from an inaccurate gust velocity input.

This frozen gust velocity input stems from PIV measurements done in the experiments at $x/c = -0.75$. These measurements have been obtained with the mounted wing whose presence

affected these measurements. This local influence of the wing on the gust measurement was investigated in this work by simulating the gust vanes simultaneously with the Delft-Pazy wing. The obtained results indicate an overprediction of the gust measurements obtained a the gust measurement point, while the influence of the wing becomes negligible at around 3.5 chord upstream of the wing. Since modelling the gust vanes with potential flow methods overpredicts the gust velocity in general, a clear quantification of this error cannot be given. We further used this gust vane modelling to explore possible limitations of the frozen gust model. While for the second case, the deviations in the structural response are negligible, we observed slight deviations for the first case for which unsteady aerodynamic effects are more dominant because of the higher gust frequency.

Lastly, this work investigated the extend of geometric nonlinearities present in the dynamic gust responses. For this nonlinear aeroelastic simulations are obtained for different gust frequencies and amplitudes. These results indicate that nonlinear effects become present but only stem from the nonlinear aeroelastic equilibrium and not the gust excitation even when targeting specifically the excitation of the first out-of-plane bending mode.

ACKNOWLEDGEMENT

The authors would like thank Cristina Riso for the structural beam model of the Delft-Pazy wing and acknowledge the contributions of J.L. Costa Fernández, A. Grille Guerra, J. Sodja, A. Sciacchitano, and B.W. van Oudheusden to the acquisition, processing and analysis of the experimental data.

8 REFERENCES

[1] Ritter, M., Hilger, J., Ribeiro, A., et al. (2024). Collaborative pazy wing analyses for the third aeroelastic prediction workshop. *AIAA Scitech 2024 Forum. Orlando, FL, USA*. doi:10.2514/6.2024-0419.

[2] Avin, O., Raveh, D. E., Drachinsky, A., et al. (2022). Experimental aeroelastic benchmark of a very flexible wing. *AIAA Journal*, 60(3), 1745–1768. doi:10.2514/1.J060621.

[3] Drachinsky, A., Avin, O., Raveh, D. E., et al. (2022). Flutter tests of the pazy wing. *AIAA Journal*, 60(9), 5414–5421. doi:10.2514/1.J061717.

[4] Palacios, R. and Cesnik, C. E. S. (2023). *Dynamics of Flexible Aircraft: Coupled Flight Mechanics, Aeroelasticity, and Control*. Cambridge Aerospace Series. Cambridge University Press.

[5] Mertens, C., Costa Fernández, J. L., Sodja, J., et al. (2023). Nonintrusive experimental aeroelastic analysis of a highly flexible wing. *AIAA Journal*, 61(7), 3062–3077. doi: 10.2514/1.J062476.

[6] Ribeiro, A. F., Casalino, D., and Ferreira, C. (2023). Free wake panel method simulations of a highly flexible wing in flutter and gusts. *Journal of Fluids and Structures*, 121, 103955. ISSN 0889-9746. doi:https://doi.org/10.1016/j.jfluidstructs.2023.103955.

[7] Kassem, A. V. (2010). *Wind Gust Generation for Wind Turbine Testing via Numerical Methods*. Master's thesis, TU Delft.

[8] Lancelot, P., Sodja, J., Werter, N., et al. (2017). Design and testing of a low subsonic wind tunnel gust generator. *Advances in Aircraft and Spacecraft Science*, 4, 125–144. doi:10.12989/aas.2017.4.2.125.

[9] del Carre, A., Muñoz-Simón, A., Goizueta, N., et al. (2019). SHARPy: A dynamic aeroelastic simulation toolbox for very flexible aircraft and wind turbines. *Journal of Open Source Software*, 4(44), 1885. doi:10.21105/joss.01885.

[10] Géradin, M. and Cardona, A. (2001). *Flexible multibody dynamics: A finite element approach*. Wiley.

[11] Simpson, R. J. and Palacios, R. (2013). Numerical aspects of nonlinear flexible aircraft flight dynamics modeling. In *54th AIAA/ASME/ASCE/AHS/ASC Structures, Structural Dynamics, and Materials Conference*. doi:10.2514/6.2013-1634.

[12] Goizueta, N., Wynn, A., and Palacios, R. (2021). Parametric krylov-based order reduction of aircraft aeroelastic models. *AIAA Scitech 2021 Forum. Online*. doi:10.2514/6.2021-1798.

[13] Shearer, C. and Cesnik, C. (2006). Modified generalized alpha method for integrating governing equations of very flexible aircraft. *47th AIAA/ASME/ASCE/AHS/ASC Structures, Structural Dynamics, and Materials Conference. Newport, Rhode Island, USA*. doi:10.2514/6.2006-1747.

[14] Murua, J., Palacios, R., and Graham, J. M. R. (2012). Applications of the unsteady vortex-lattice method in aircraft aeroelasticity and flight dynamics. *Progress in Aerospace Sciences*, 55, 46–72. doi:10.1016/j.paerosci.2012.06.001.

[15] Morino, L. and Bernardini, G. (2001). Singularities in bies for the laplace equation; joukowski trailing-edge conjecture revisited. *Engineering analysis with boundary elements*, 25(9), 805–818. doi:10.1016/S0955-7997(01)00063-7.

[16] Simpson, R. J., Palacios, R., and Murua, J. (2013). Induced-drag calculations in the unsteady vortex lattice method. *AIAA journal*, 51(7), 1775–1779.

[17] Düssler, S. and Palacios, R. (2024). Enhanced unsteady vortex lattice aerodynamics for nonlinear flexible aircraft dynamic simulation. *AIAA Journal*, 62(3), 1179–1194. doi:10.2514/1.J063174.

[18] Katz, J. and Plotkin, A. (2001). *Low-speed aerodynamics*, vol. 13. Cambridge University Press.

[19] Goizueta Alfaro, N. (2022). *Parametric reduced-order aeroelastic modelling for analysis, dynamic system interpolation and control of flexible aircraft*. Ph.D. thesis, Imperial College London.

[20] Maraniello, S. and Palacios, R. (2019). State-space realizations and internal balancing in potential-flow aerodynamics with arbitrary kinematics. *AIAA Journal*, 57(6), 2308–2321. doi:10.1088/1742-6596/1037/2/022033.

[21] Mertens, C., Sciacchitano, A., van Oudheusden, B. W., et al. (2021). An integrated measurement approach for the determination of the aerodynamic loads and structural motion for unsteady airfoils. *Journal of Fluids and Structures*, 103, 103293.

[22] Sanghi, D., Riso, C., and Cesnik, C. (2024). Evaluation of aeroelastic models for gust response prediction in very flexible wingst. *International Forum on Aeroelasticity and Structural Dynamics, IFASD, The Hague, Netherlands*.

[23] Riso, C. and Cesnik, C. E. (2021). Correlations Between UM/NAST Nonlinear Aeroelastic Simulations and the Pre-Pazy Wing Experiment. *AIAA Scitech 2021 Forum. Online*. doi:10.2514/6.2021-1712.

[24] Goizueta, N., Wynn, A., Palacios, R., et al. (0). Flutter predictions for very flexible wing wind tunnel test. *Journal of Aircraft*, 0(0), 1–16. doi:10.2514/1.C036710.

[25] Etkin, B. (1981). Turbulent wind and its effect on flight. *Journal of Aircraft*, 18(5), 327–345. doi:10.2514/3.57498.

COPYRIGHT STATEMENT